Laboratory measurements of water saturation effects on the acoustic velocity and attenuation of sand packs in the 1–20 kilohertz frequency range

Hanif S. Sutiyoso[a,b], Sourav K. Sahoo[b], Laurence J. North[b], Timothy A. Minshull[a] , Ismael Himar Falcon-Suarez[b], Angus I. Best[b]

[a] *School of Ocean and Earth Science, University of Southampton, Waterfront Campus, European Way, Southampton SO14 3HZ, UK*

[b] *National Oceanography Centre, European Way, Southampton SO14 3HZ, UK*

Abstract

We present novel experimental measurements of acoustic velocity and attenuation in unconsolidated sand with water saturation within the sonic (well-log analogue) frequency range of 1 – 20 kilohertz. The measurements were conducted on jacketed sand packs with 0.5-metre length and 0.069- metre diameter using a bespoke acoustic pulse tube (a water-filled, stainless steel, thick-walled tube) under 10 Megapascal of hydrostatic confining pressure and 0.1 Megapascal of atmospheric pore pressure. We assess the fluid distribution effect on our measurements through an effective medium rock physics model, using uniform and patchy saturation approaches. Our velocity and attenuation (Q^{-1}) are accurate to ± 2.4% and ± 5.8%, respectively, based on comparisons with a theoretical transmission coefficient model. Velocity decreases with increasing water saturation up to ~75% and then increases up to the maximum saturation. The velocity profiles across all four samples show similar values with small differences observed around 70-90% water saturation, then converging again at maximum saturation. In contrast, the attenuation increases at low saturation followed by a slight decrease towards maximum saturation. Velocity increases with frequency across all samples, which contrasts with the complex frequency-dependent pattern of attenuation. These results provide valuable insights into understanding elastic wave measurements over a broad frequency spectrum, particularly in the sonic range.

Keywords: acoustics, pulse tube, velocity, attenuation, rock physics, modelling

1. Introduction

Accurate characterisation of sub-seafloor geological features using seismo-acoustic methods is crucial for hydrocarbon exploration (e.g., Asada et al., 2022; Ellingsrud et al., 2002), carbon dioxide and energy storage (e.g., Fawad and Mondol, 2021; Li et al., 2020), and marine geotechnical surveys (e.g., pipelines or windfarms) (Le et al., 2014; Reynolds et al., 2017). These imaging methods can provide useful information on stratigraphy (e.g., folds, faults) and fluid distribution, deriving physical properties from elastic wave velocity and attenuation. Understanding controls on the compressional (P-) and shear (S-) wave properties of marine sediments at sonic frequencies of 1-20 kilohertz (kHz) can help interpretation of high-resolution seismic surveys, such as Chirp sub-bottom profilers operating in the 1–10 kHz frequency range (McCann et al., 2014). In addition, knowledge of these properties at elevated confining pressures and temperatures can help the interpretation of data from borehole sonic logs operating at 10 – 15 kHz in more deeply buried sediments.

P-wave velocity and attenuation are sensitive to fluid content and pore connectivity (Mavko et al., 2009); while S-wave velocity remains insensitive unless fluid density changes. Therefore, most studies focus on P-wave properties when investigating water saturation effects. The relationship between fluid content and elastic wave properties is often complex, representing a challenge to interpreting seismo-acoustic data. This relationship can be quantified in a laboratory setting where environmental conditions can be controlled. For instance, resonant bar studies have shown that partial liquid saturation creates strong attenuation in porous rocks in the kHz range (e.g. Batzle et al., 2006; Chapman et al., 2021; Murphy, 1982). At sonic frequencies, compacted heterogeneous soils evidence similar velocity and attenuation versus water saturation dependencies to rocks (e.g., Barriere et al., 2012; Cadoret et al., 1998; Dong et al., 2023). However, there are few studies on saturation effects at sonic frequencies, especially in unconsolidated sediments with varying water saturation (McCann et al., 2014). Most prior research focused on dry or nearly fully saturated media (Ayres and Theilen, 2001; Prasad, 2002).

Theoretical model studies by Biot, Stoll (e.g., (Biot, 1956a, 1956b; Stoll, 1985) and others have investigated fluid content effects on elastic wave properties. Biot's theory describes how elastic waves induce frequency-dependent fluid motion relative to the solid matrix in porous media, influenced by fluid viscosity, density, and rock matrix permeability, leading to frequency-dependent velocity and attenuation. The theory predicts two compressional waves (fast and slow) and a shear wave, with the slow P-wave being highly attenuated and rarely observed (e.g., Bouzidi and Schmitt, 2009). Other theoretical studies have examined gas and liquid distribution effects, whether uniform or patchy (e.g., Pride et al., 2004; White, 1975).

We conducted an experimental study to investigate the effects of water saturation on frequency-dependent compressional wave velocity and attenuation (expressed as the inverse quality factor, Q^{-1}) in unconsolidated sand packs at sonic frequencies. These sand packs are known to conform well to Biot's model description of wave propagation, at least in saturated samples at ultrasonic frequencies (e.g., Klimentos and McCann, 1988). We used a water-filled acoustic pulse tube similar to the one described by McCann et al. (2014) to measure P-wave velocity and attenuation on sediment samples (0.5 m length, 0.069 m diameter) at 1 – 20 kHz. We compared our pulse tube data with an effective medium rock physics model (i.e., the Biot-Stoll model) to understand the underlying mechanisms.

Our measurements can be used to validate frequency-dependent rock physics models, which are important for accurately interpreting subsurface properties. The intermediate (sonic) frequency range that lies between ultrasonic and seismic frequencies is often key to understanding theoretically predicted velocity dispersion and attenuation peaks caused by visco-elastic relaxation that tend to occur in this range (Guerin and Goldberg, 2005; Sahoo and Best, 2021). These models, potentially modified to account for our data, can then be used to interpret field seismic (including the high-resolution method) and borehole sonic log data in relation to pore fluid content analysis. For example, enhanced rock physics models can facilitate monitoring of carbon storage, from the sequestration process, which can introduce patchy saturation, to detecting seabed gas leaks (Azuma et al., 2013; Jedari-Eyvazi et al., 2023).

2. Methods

2.1. Sample Preparation and Measurement Procedure

The samples comprised clay-free quartz sand from Leighton Buzzard with a mean grain diameter of 100 μm. We used polyvinyl chloride (PVC) material to make cylindrical jackets (outer diameter 0.069 m, inner diameter 0.063 m, length 0.5 m) and endcaps to hold the sand and enable sample emplacement within the water-filled pulse tube (Figure 1). The PVC's acoustic impedance is 2.9 x 10^6 kg m^{-2} s^{-1} with a velocity of 2600 m s^{-1} and density of 1120 kg m^{-3} (Selfridge, 1985), similar to that of water-saturated sand: 2.2 - 4.2 x 10^6 kg m^{-2} s^{-1} with a velocity of 1450 – 2200 m s^{-1} and density of 1460 – 1890 kg m^{-3} (Schumann et al., 2014). We sealed both ends of the jacket using 3-cm thick PVC endcaps with attached O-rings. These endcaps were free to move lengthways inside the jacket while maintaining a pressure seal, thus allowing the external surrounding water confining pressure to be applied evenly to the sand pack inside the pulse tube.

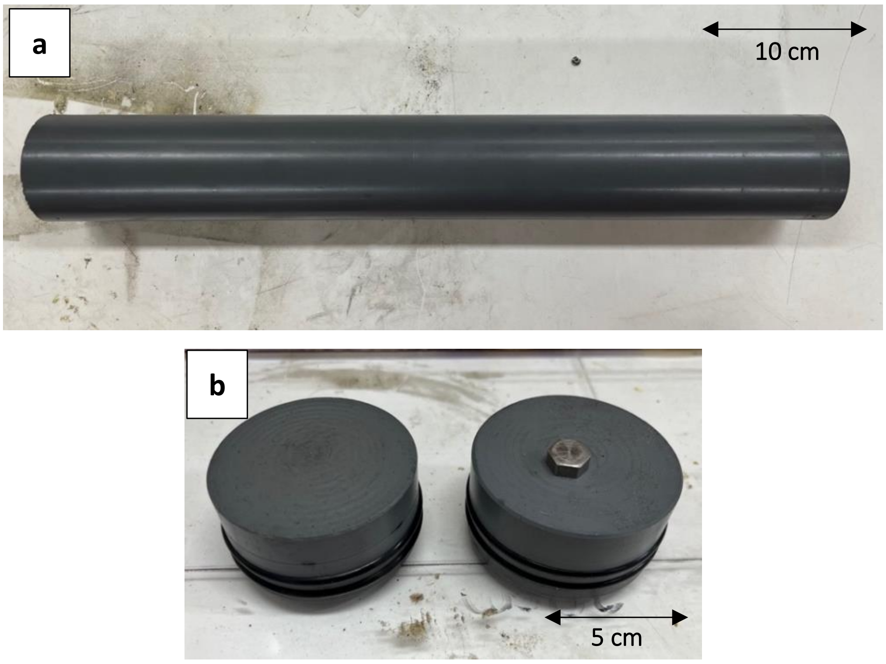

Figure 1 Components of jacket system used to hold the sand pack: a) 50 cm length PVC cylinder jacket, and b) top and bottom PVC endcaps with O-ring seals and location of pore fluid vent port (hexagonal nut on top endcap on the right).

To avoid inconsistencies during the preparation of sand packs that could cause significant density and porosity variations along the sample, we developed a repeatable sample preparation procedure. First, we oven-dried the sediment in a 60°C oven for 24 hours, then we tamped and evenly compacted the sand in successive layers into the cylindrical jacket, with the bottom endcap fitted beforehand, mimicking the "Proctor method" for compacting soils (ASTM, 2007). We provide further explanation in the Supplementary Information. Finally, we fitted the top cap to prevent leaks and inserted the dry sample into the pulse tube for measurements under dry conditions.

We measured sample mass and dimensions before each experiment and calculated sample porosity ($\emptyset$) based on grain density and sample densities (ρ_d and ρ_b, respectively), as $\emptyset = 1 - \frac{\rho_b}{\rho_d}$. The porosity of the four samples (A-D) ranges from 38% to 44%, as shown in Table 1.

Table 1 Experimental parameters of sand pack samples.

<table>
<tr><th>Sample</th><th>Porosity (%)</th><th>Water Saturation (%)</th><th>Effective Pressure (MPa)</th></tr>
<tr><td>A</td><td>38 ± 0.25</td><td rowspan="4">0-100</td><td rowspan="3">10</td></tr>
<tr><td>B</td><td>40 ± 0.25</td></tr>
<tr><td>C</td><td>44 ± 0.25</td></tr>
<tr><td>D</td><td>42 ± 0.25</td><td>0, 1, 5, 10</td></tr>
</table>

We used de-ionised water in the water saturation experiments. Firstly, we connected a vacuum pump to the downstream pore fluid port to remove air from the sample. Upon constant vacuum pressure, we opened the upstream port to enable water imbibition from an external reservoir. Simultaneously, we recorded the mass change in the reservoir to estimate the pore water volume, and hence the water saturation (i.e., water to pore volume ratio). We repeated this process to achieve several water saturation steps, up to 30%. Above this point, the vacuum method was inefficient, so we switched to imbibition, allowing better control of the saturation process at a higher saturation range. Imbibition relies on the capillary pore fluid pressure at the interface between the gas and liquid to draw in more liquid until full saturation is reached (McPhee et al., 2015). For each saturation step, we placed the sample vertically in a water-filled acrylic container for 48 hours with the water level just above the top cap with two openings to provide water ingress. We tilted the container to around 45 degrees and rotated the sample every 3 to 4 hours to evenly distribute the water inside the pore space under gravity. Then, we weighed the sample again to measure the added mass of water and new saturation. We aimed to add 50 - 60 mL of water for each saturation step.

As an extra measure to understand the water distribution in the sample, we utilised an experimental microwave scanner (Fig. 2; Section 2.2). If the water distribution was not uniform, we left the sample for another 24 hours for the water to distribute further before being placed in the pulse tube for measurements. We repeated the water addition procedure until the sample was fully saturated for each sample. Please refer to Figure 5a for the complete workflow of sample preparation and pulse tube data acquisition.

2.2. Water Saturation Monitoring using the Microwave Method

Understanding the water distribution inside the sand sample is essential to interpreting pulse tube results. Hence, we developed a novel microwave measurement technique to achieve that understanding. Microwave methods have been widely utilised to measure the water content of soil, e.g., from measurements of electrical permittivity or dielectric constant (e.g., Richards et al., 2014). They are non-destructive methods and thus can preserve the sample condition.

We used a free-space, contactless, microwave method to monitor the water distribution utilising a vector network analyser with two spot-focusing, curved antennae in the 1 – 6 GHz frequency range. We used a PicoVNA 106 Quad RX with a frequency resolution under 10 kHz. In general, a Vector Network Analyser (VNA) is used to test materials by applying a test signal to the materials, measuring the reflected and transmitted signals, and then comparing them to the test signal. In our method, we only used the transmission signals to determine the water saturation. The system was connected to a PC to run the measurements using PicoVNA2 software (Figure 2a-b).

This microwave method requires an accurate calibration between the measured dielectric permittivity and the actual water content of the soil (Ghodgaonkar et al., 1990), so we conducted an in-house calibration. We obtained reference values for the dielectric permittivity of saturated and dried samples in the 1-6 GHz frequency range using a shorted coaxial cell, consisting of a coaxial structure where the inner conductor is short-circuited to the outer conductor at one end to maximise the microwave reflection, which is critical for determining accurately the dielectric properties of the sample material. The cell, with an internal diameter of 16 mm and a centre conductor diameter of 7 mm, measures 55 mm in axial length (Figure 2c). The cell calibration was performed using a multiple-offset short method (Glasser, 1978).

Leighton Buzzard sand was saturated with RO water in a container outside the coaxial calibration cell, and then lightly compacted into the coaxial cell for measurement. Subsequently, the saturated sample underwent oven drying at 60°C for 48 hours and was re-measured to determine the dielectric constant for the dry sample. The cell and its contents were weighed in both saturated and dry states to calculate saturation and pore volume gravimetrically, assuming a grain density of 2650 kg m^{-3}. The pore volume of the sample was 42%, typical of uncompacted sand, with a water saturation of 88.75%. We calibrated the system by measuring the dielectric constant of dry and fully saturated sand, 2.5 and 22.6 F m^{-1}. Peak picking of wideband transmitted signal arrival time is used to calculate group velocity and hence dielectric constant. A comparison between the dielectric constant for dry sand and air obtained with the coaxial cell and antenna measurement system allowed us to deduce error bounds for the antenna system, conservatively set at a 10% error margin. We used these dielectric constant values to obtain the water saturation as described in the Supplementary Information.

We monitored the water distribution in the PVC-jacketed sand samples by conducting a microwave reading at 5 cm intervals down the length of all samples after each water addition step. We defined the distribution from the standard deviation of the measured water saturations down the sample. If the standard deviation of saturation values determined in the sample was over 15%, we left the sample for another 24 hours to let the water evenly distribute and repeated the readings until the requirement was fulfilled. An example of the water distribution of the sample at several saturation levels is provided in Figure 3.

As the saturation increases, a more uniform water distribution is easier to achieve. At most saturations, the bottom half of the sample (0-25 cm) tends to saturate first due to the influence of gravity on the imbibition process. This phenomenon is particularly clear at intermediate saturations, as illustrated by the orange and yellow lines in Figure 3. This higher saturation extends from 5-10 cm (orange lines) and up to 25 cm (yellow lines), potentially affecting the acoustic properties at higher frequencies where the acoustic wavelength is shorter than the region of higher saturation. To assess this effect, we calculated the wavelength from the velocity and frequency ($wavelength = velocity / frequency$). We found that the lengths of the regions with higher saturation correspond to the wavelength for frequencies higher than 12 kHz (~11 cm wavelength; orange line) and 6 kHz (~21 cm wavelength; yellow line). Further discussion of the effect of variable water saturation at different frequencies is provided in Section 3.1.

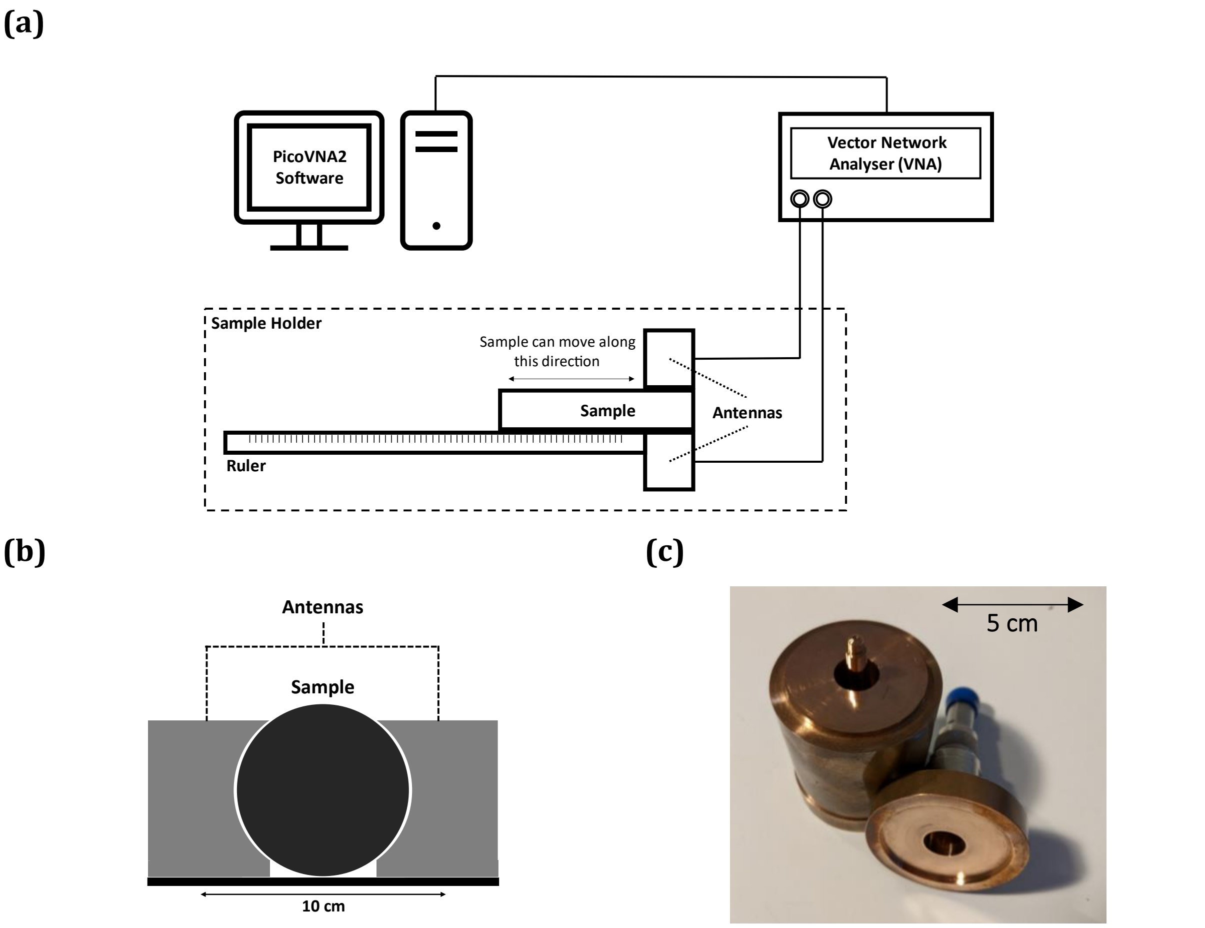

Figure 2 Block diagram of the experimental microwave setup: a) complete setup connecting to computer, and b) side-view of the microwave setup. c) Coaxial cell used for calibration measurements. Photographs of the microwave setup are provided in the Supplementary Information (Figure S4).

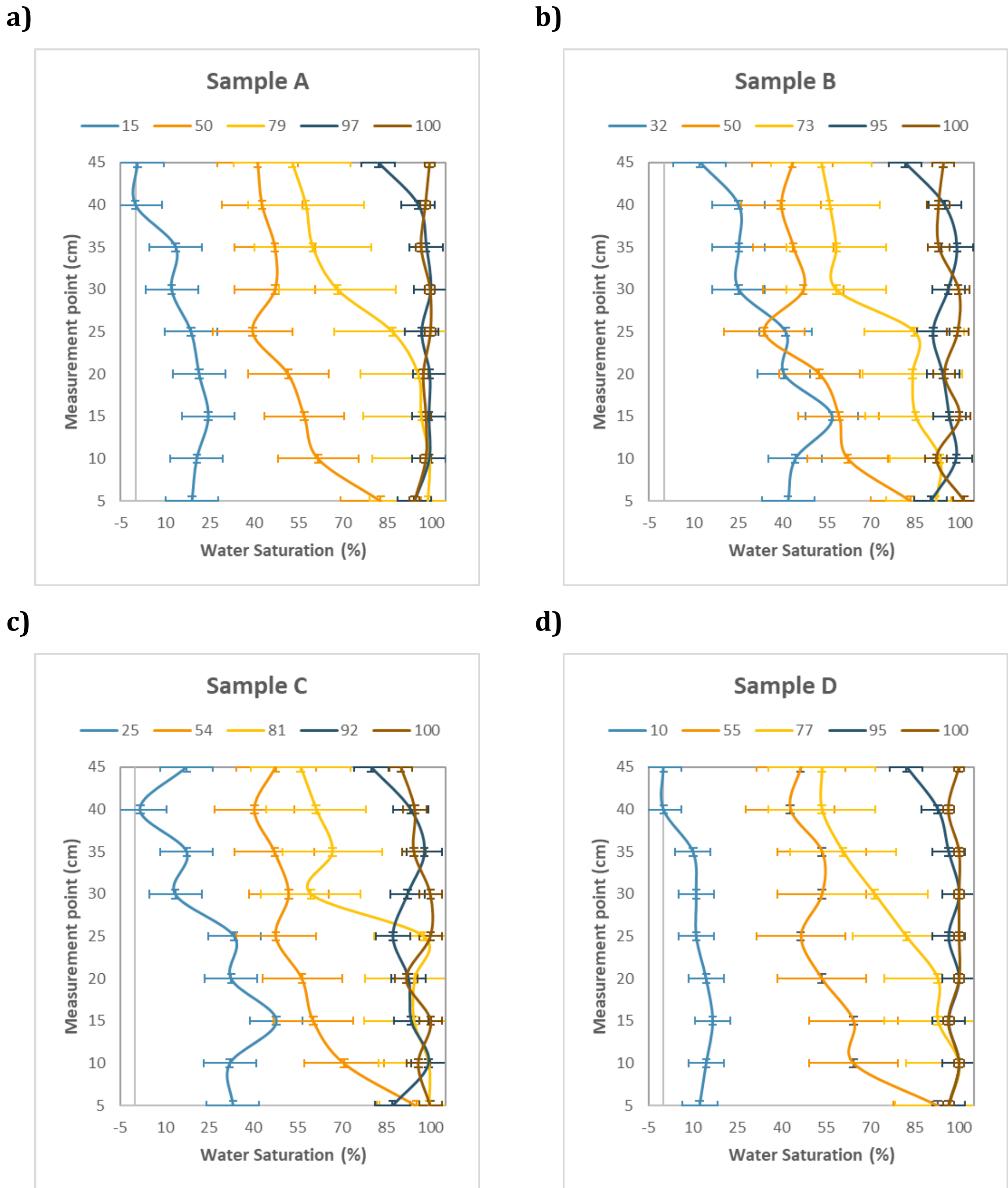

Figure 3 Water saturation distributions for progressively increasing % sample saturations (see legend) using the microwave transmission system for all samples with error bars at various saturations (a, b, c, d). The readings are every 5 cm along the sample. The top (50 cm) and bottom (0 cm) measurements are not calculated due to the influence of the PVC end caps on microwave readings. The standard deviation for each sample is 9.9, 10.9, 12, and 9.5% (Sample A to D). The differences between the microwave readings and the water saturation values calculated from sample weight are 6.0, 6.2, 6.6, and 4.8% (Sample A to D).

2.3. Acoustic Pulse Tube

2.3.1. Experimental Apparatus

The acoustic pulse tube utilises an acoustic waveguide concept consisting of a water-filled, thick-walled, stainless steel cylindrical tube. This setup is common for investigating acoustic properties of materials using the theory of axially propagating plane waves in a fluid-filled, rigid-walled waveguide. The pulse tube has a waveguide diameter of 0.07 m, and no higher modes will propagate at frequencies less than 26 kHz (McCann et al., 2014). McCann et al. (2014) also argued based on the theory of Dubbelday and Capps (1984) that plane waves propagate in the sediment-jacket system. The ratio of the tube radius to the sample radius should be smaller than 1.03 for a low-impedance material, such as our sediment-jacketed system. In our experiment, the ratio is 1.014, below this critical value.

We conducted the experiment using a 4.5 m long pulse tube at the National Oceanography Centre (NOC), Southampton (Figure 4). The tube has an inner diameter of 0.07 m with the capacity to hold a sample with a diameter of 0.069 m. The designed maximum confining pressure of the pulse tube vessel is 60 MPa, though for this study, we only tested at a confining pressure below 12.5 MPa. A water circulation jacket that wraps the vessel is connected to a temperature control unit, allowing an experimental temperature within the range of -5 to 55°C. We performed the measurements for all samples at a controlled temperature of 4°C and a confining pressure of 10 MPa with a pore fluid port connected to the sample vented to atmospheric pressure through the pulse tube top cap, thus giving an effective (differential) pressure of c. 10 MPa, analogous to subsurface depths of about 1 kilometre in the earth. We also performed measurements on sample D at increasing effective pressures (Table 1).

A bespoke acoustic piezo-electric transducer located at the bottom of the pulse tube insonified the jacketed sample in the 1-20 kHz range using variable-frequency chirp signals (i.e., within the working frequency of well logs). The pulse tube has two hydrophones installed through side-wall ports at a spacing of 1.2 m. The sample is suspended between the hydrophones, hanging from the top cap through the pore fluid line. We acquired the data using an Agilent 30 MHz Function/Arbitrary Wave generator producing a 6-second 20 kHz chirp synchronised to a LeCroy WaveSurfer 200 MHz

Oscilloscope to display and record the output. We stacked the readings 16 times to improve the signal-to-noise ratio.

The confining and pore pressure are controlled by an ISCO EX-100D syringe pump system. To minimise undesired distortions of the signal associated with trapped air, first, we slowly lowered the jacketed sample into the tube using the pore fluid pipe, ensuring no air bubbles were trapped at the bottom of the sample. Then, we systematically increased the confining pressure and opened valves in the top cap of the pulse tube to release any air trapped inside the sample. Lastly, we closed the pulse tube with its top cap and slowly elevated (~0.01 MPa/s) the confining pressure to the target pressure. We stabilised the pulse tube system for ~2 hours to let the sand sample equilibrate. After completing the measurements, we released the confining pressure at the same rate as before to prevent the sample from experiencing any stress-release-induced damage before removing the sample. Additionally, we measured the water-filled pulse tube without any sample as a reference for the acoustic data processing and calibration.

2.3.2. Acoustic Data Processing

The measurements comprised time series of signal amplitude (voltage) from the sample at each saturation and from the water-filled pulse tube. The time-domain data were transformed into the frequency domain using a Fast Fourier Transform (FFT) to then deconvolve the raw signals with the chirp source signal, thus obtaining the impulse response. The stimulus is monochromatic (i.e., single frequency), thus the equations used in the processing are evaluated at each frequency coincident with those of the FFT of the measured gated time domain signal.

We applied time-domain gating to eliminate multiple reflections from the pulse tube endcaps, although any reflections that coincide temporally with the time-domain gate may degrade results. These are typically proximal reflections from geometrical changes in the pulse tube, for instance, the hydrophone ports along the pulse tube. Figures 5b and 6 show the data processing workflow and examples of the raw and processed time-domain data.

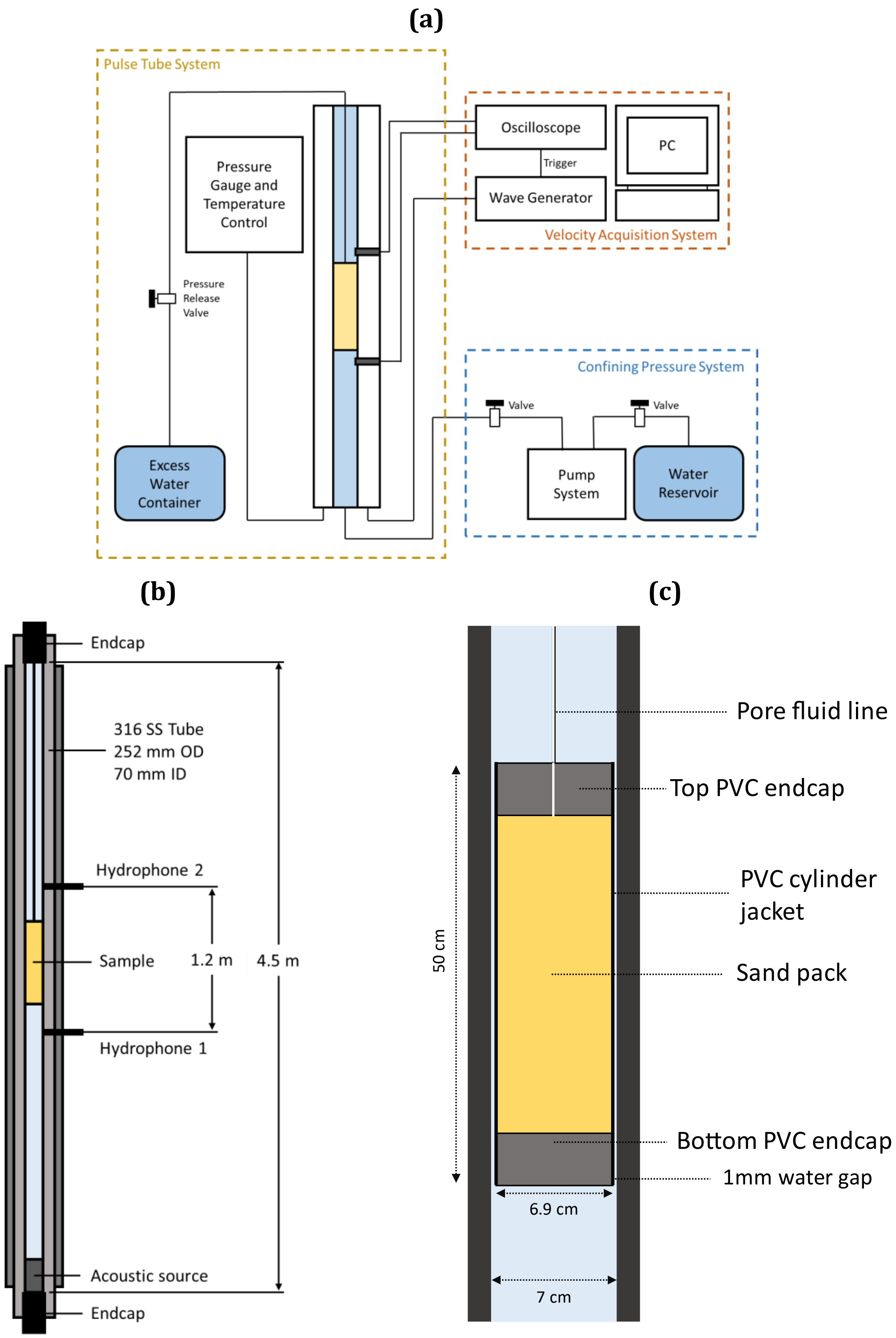

Figure 4 Diagram of the experimental pulse tube setup: a) Schematic diagram of pulse tube with pressure system and data acquisition setup, b) Dimensions of the pulse tube in detail, and c) Detail of the PVC-jacketed sample inside the pulse tube with pore fluid line (vented via high-pressure lead-throughs in the top cap of the pulse tube).

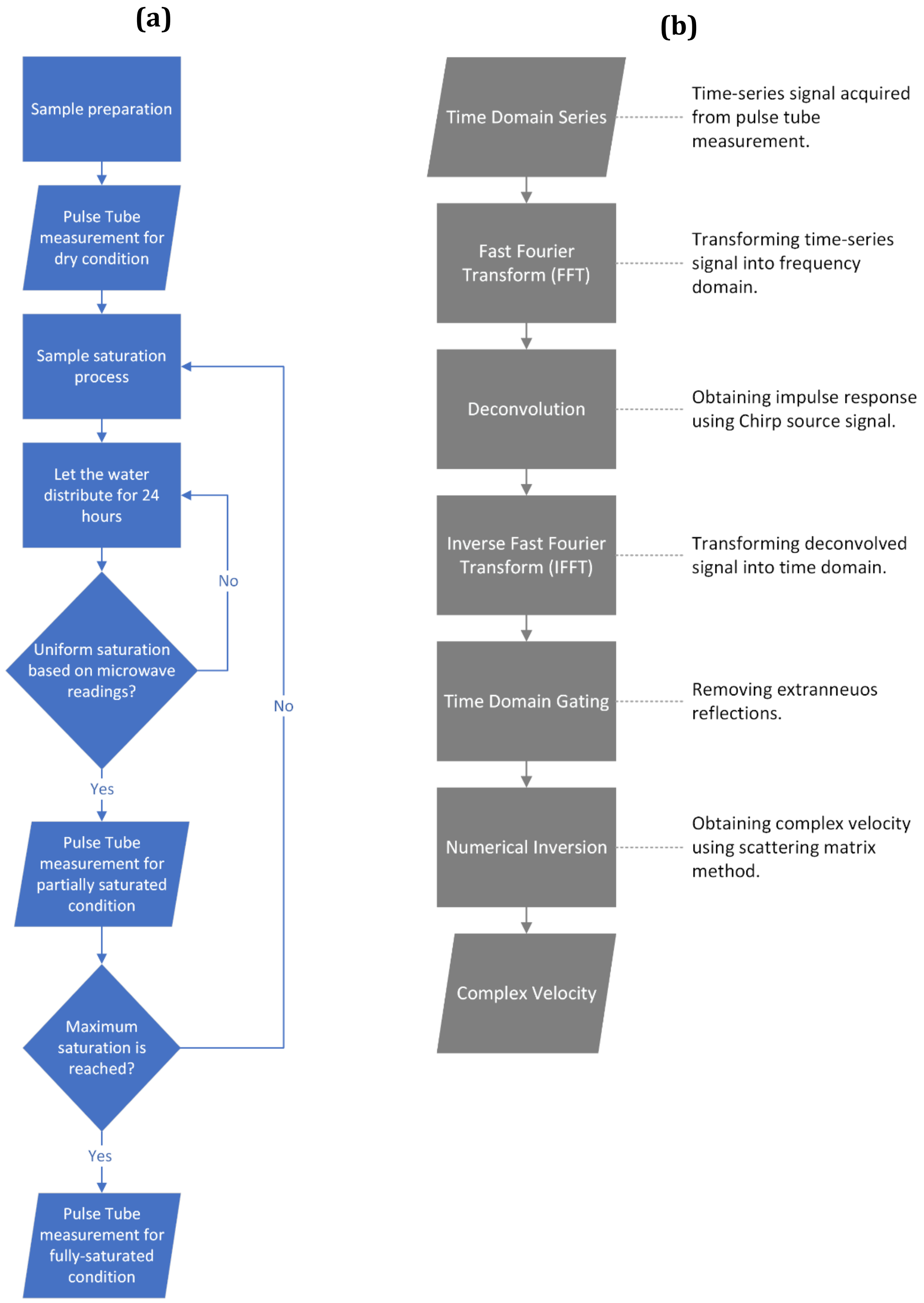

Figure 5 Workflow diagrams for: (a) sample preparation and pulse tube data acquisition, and (b) data processing steps (with description) to obtain the acoustic wave properties.

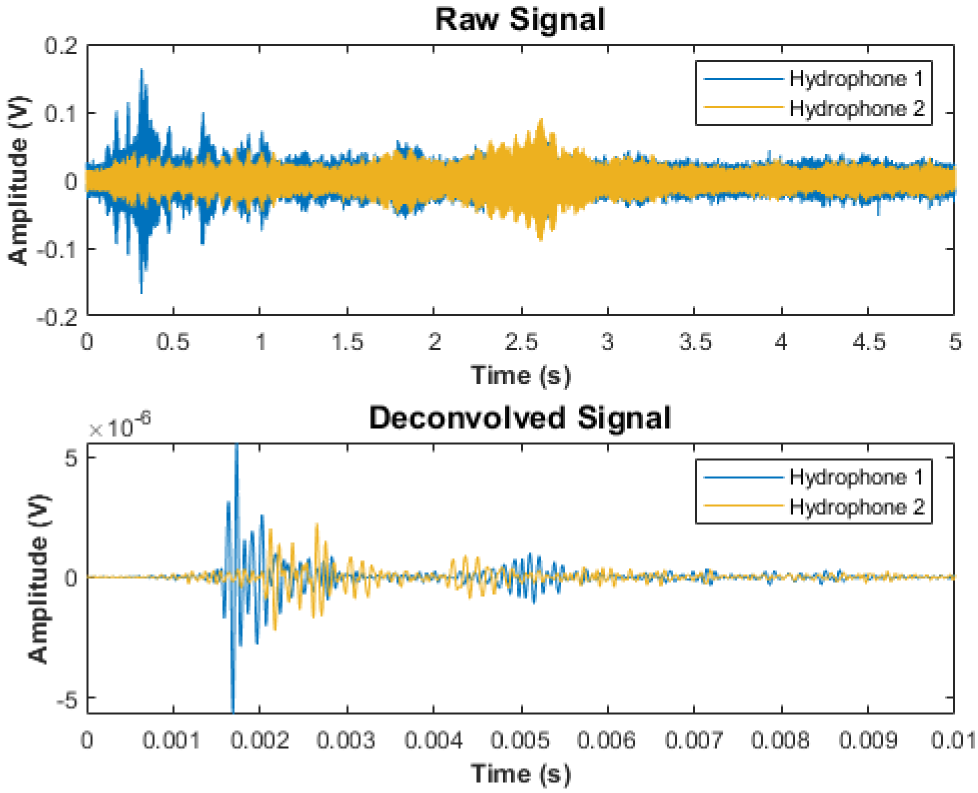

Figure 6 An example of raw and deconvolved time-domain acoustic data on a jacketed sand sample (Sample D) from pulse tube measurements. The positions of hydrophones 1 and 2 are shown in Figure 4. Further examples for different samples are provided in the Supplementary Information (Figure S2 and S3).

We used nonlinear inversion to minimise the following objective function, which uses an initial value estimated using the time domain signal, thus deriving the complex velocity of the sample. We assumed a linear time-invariant system to ensure the input and output are scaled by the same value. We also assumed a plane wave propagation so that shear moduli of the sample (i.e., sand pack) and end caps may be neglected, resulting in a one-dimension transmission line system without any propagation at the sidewalls, multiple paths, or shear-wave coupling. The main objective function is provided in Equation 1, while the analytical descriptions are provided in Equations 2-13 and illustrated in Figure 7.

$$Objective\ function = |R_{1mod} - R_{1obs}| + |R_{2mod} - R_{2obs}| \tag{1}$$

$$R_{1mod} = \frac{m_1}{m_{1ref}} \tag{2}$$

$$R_{2mod} = \frac{m_2}{m_{2ref}} \tag{3}$$

$$R_{1obs} = \frac{M_1}{M_{1ref}} \tag{4}$$

$$R_{2obs} = \frac{M_2}{M_{2ref}} \tag{5}$$

With m_1 and m_2 as follows:

$$m_1 = Ph_1 \left[(1 + \gamma_{w1}^2 S_{11c1}) + \gamma_{w1}^2 \gamma_s^2 S_{21c1} S_{12c1} S_{11c2} \sum_{n=0}^{n=\infty} \gamma_s^{2n}\, S_{22c1}^n S_{11c2}^n \right] \tag{6}$$

$$m_2 = Ph_2 \left[(\gamma_{w1}\gamma_{w2}\gamma_s S_{21c1} S_{21c2}) \sum_{n=0}^{n=\infty} \gamma_s^{2n}\, S_{22c1}^n S_{11c2}^n \right] \tag{7}$$

By using the concept of infinite geometric series, we could simplify Equations 6-7 into Equations 8-9.

$$m_1 = Ph_1 \left[(1 + \gamma_{w1}^2 S_{11c1}) + \frac{\gamma_{w1}^2 \gamma_s^2 S_{21c1} S_{12c1} S_{11c2}}{1 - \gamma_s^2 S_{22c1} S_{11c2}} \right] \tag{8}$$

$$m_2 = Ph_2 \left[\frac{\gamma_{w1}\gamma_{w2}\gamma_s S_{21c1} S_{21c2}}{1 - \gamma_s^2 S_{22c1} S_{11c2}} \right] \tag{9}$$

And m_{1ref} and m_{2ref} as follows:

$$m_{1ref} = Ph_1 \tag{10}$$

$$m_{2ref} = Ph_2 \gamma_{w1}\gamma_{w2}\gamma_{w3} \tag{11}$$

P is the incident stimulus, h_1 and h_2 are the hydrophones transfer functions. γ is the transmission coefficient and S represents the scattering matrix. Small m- stands for the inversion model while big M stands for the actual measurement with ref notation referring to water-filled tube condition (without sample).

Lastly, by taking the ratio R_{1mod} and R_{2mod}, we could remove P, h_1 and h_2, as provided in Equations 12-13. The complete description of the scattering parameters is provided in the Supplementary Information.

$$R_{1mod} = (1 + \gamma_{w1}^2 S_{11c1}) + \frac{\gamma_{w1}^2 \gamma_s^2 S_{21c1} S_{12c1} S_{11c2}}{1 - \gamma_s^2 S_{22c1} S_{11c2}} \tag{12}$$

$$R_{2mod} = \frac{1}{\gamma_{w3}} \frac{\gamma_s S_{21c1} S_{21c2}}{1 - \gamma_s^2 S_{22c1} S_{11c2}} \tag{13}$$

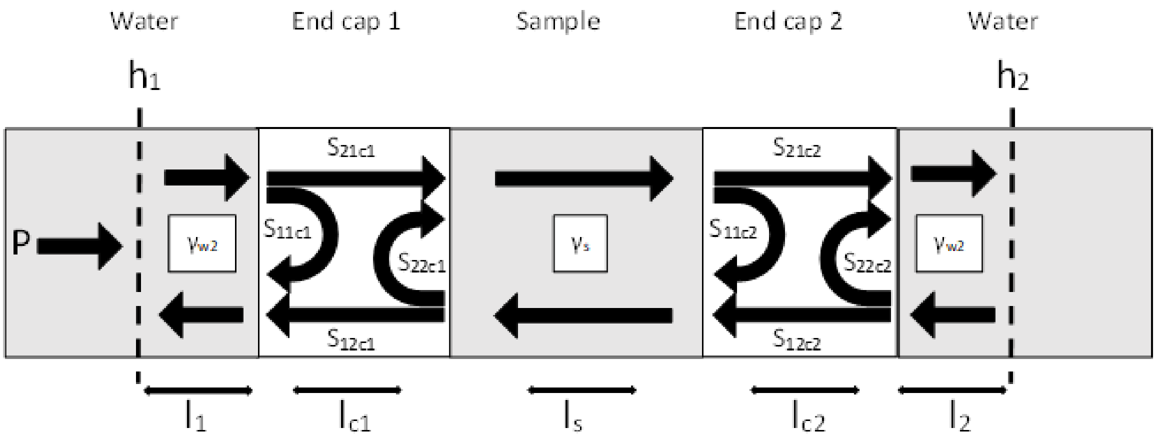

Figure 7 Description of scattering parameters used in the idealised transmission line (scattering matrix) model of the acoustic pulse tube that are included in the numerical inversion. Refer to the Supplementary Information for the mathematical definition of symbols.

We calculated the attenuation Q^{-1} from the real and imaginary velocity output of the scattering matrix method using Equation 14 (Mavko et al., 2009).

$$Q^{-1} = \frac{1 - e^{-2\pi\frac{v_1}{v_2}}}{2\pi} \tag{14}$$

where v_1 and v_2 are the real and imaginary velocities, respectively.

2.3.3. Acoustic Pulse Tube Calibration

The calibration process involved several steps. First, we determined the velocity and attenuation errors by comparing the pulse tube and theoretical transmission coefficients (McCann et al., 2014). The theoretical model predicts the sample's response based on plane wave transmission through an infinite plate of finite thickness L and the acoustic impedance of the sample I_2 inside a fluid with acoustic impedance I_1 as defined in Equations 15-17. We determined the error bounds as the parameter values at which the sum of squares of the residuals between experimental and theoretical transmission coefficients reached 10% higher than the best-fit solution.

$$T = \frac{4I_1I_2}{(I_1 + I_2)^2 e^{ik_2L} - (I_1 - I_2)^2 e^{-ik_2L}} \tag{15}$$

$$k_2 = 2\pi\left(\frac{f}{V_2} - \frac{if}{2QV_2}\right) \tag{16}$$

$$I_2 = \rho_2 \frac{2\pi f}{k_2} \tag{17}$$

where T is the transmission coefficient of compressional waves, k_2 is the wavenumber of the sample, V_2 is the velocity of the sample, and f is frequency.

Firstly, we used a material with well-known properties, i.e., a nylon rod, to calibrate our method. Then, we used the same method on the PVC jacketed sand packs. The comparisons are in good agreement based on R^2 (or the coefficient of determination) values of 0.95 and 0.89, showing that 95% and 89% of the variance of the experimental data was accounted for by the theoretical model for nylon and PVC-jacketed samples, respectively (Table 2 and Figure 8).

Table 2 Errors of pulse tube measurements on two samples calculated from the comparison of pulse tube transmission coefficient with theoretical models. R^2 is the coefficient of determination for the transmission loss (Figure 8).

Sample	Velocity (m s^{-1})	Attenuation (Q^{-1})	R^2
Nylon	± 1 %	± 3.9 %	0.95
PVC with sand	± 2.4 %	± 5.8 %	0.89

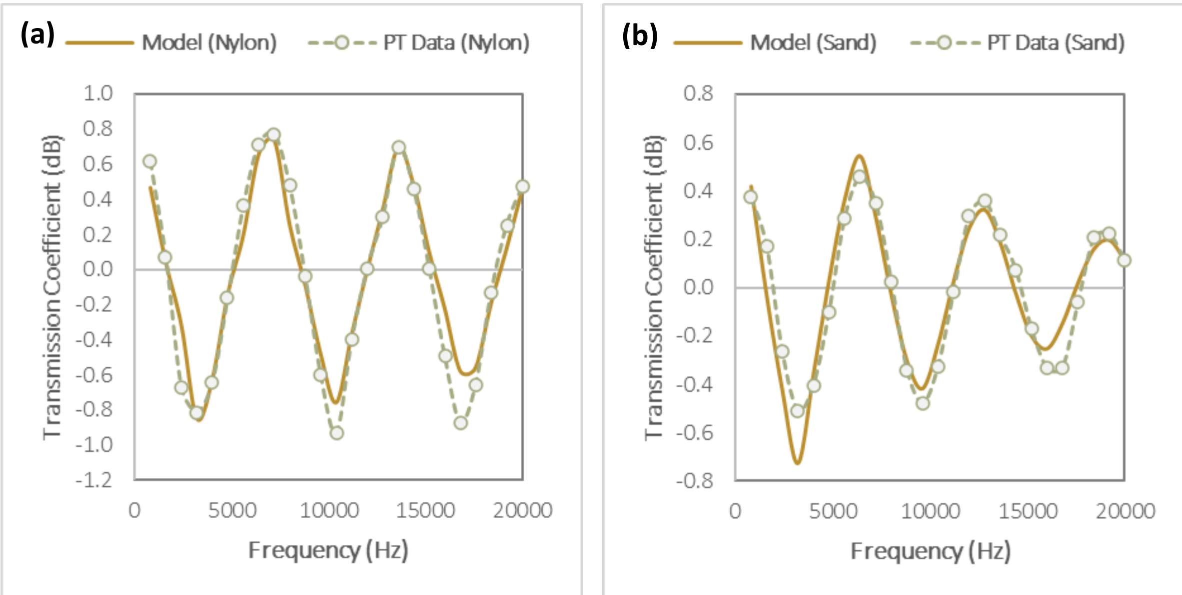

Figure 8 Experimental and theoretical transmission loss coefficient spectra (in dB) for: a) nylon and b) jacketed sand at an effective pressure of 10 MPa and temperature of 4°C. Dashed lines with points represent pulse tube data and solid lines represent the theoretical result from the transmission model.

The error is slightly higher in the PVC-jacketed sample compared to the nylon rod, perhaps because of the multi-layered system of the jacketed sample, i.e., end caps and PVC tube with the sample inside. This layering could affect the propagating wave by introducing complexity in the scattering matrix calculation, compared to the solid nylon rod without any jacket and end caps.

Next, we compared our data to those reported by Selfridge (1985) for nylon at ultrasonic frequencies. We converted Selfridge's ultrasonic data to sonic frequency, i.e., from 0.5 MHz to 10 kHz, using Equation 18 from Kolsky (1956).

$$Vp(f_1) = Vp(f_2)\left[1 + \frac{1}{\pi Q}\ln\left(\frac{f_1}{f_2}\right)\right], \quad (18)$$

where $Vp(f_1)$, $Vp(f_2)$ are the nylon compressional wave velocities at frequencies f_1 and f_2 respectively, and Q is the quality factor measured by Selfridge, which is assumed constant in the frequency range from f_1 to f_2.

Table 3 Acoustic properties of nylon from pulse tube measurements and from the ultrasonic measurements of Selfridge (1985).

<table>
<tr><th colspan="2">Pulse tube observation</th><th colspan="2">Ultrasonic P-wave observation</th></tr>
<tr><th>Velocity (m s^{-1})</th><th>Q^{-1}</th><th>Velocity (m s^{-1})</th><th>Q^{-1}</th></tr>
<tr><td>2546 ± 25</td><td>0.008 ± 0.0005</td><td>2600</td><td>0.006</td></tr>
<tr><td colspan="4">Velocity comparison</td></tr>
<tr><th colspan="2">Pulse tube (m s^{-1})</th><th colspan="2">Corrected ultrasonic measurement (m s^{-1})</th></tr>
<tr><td colspan="2">2546 ± 25</td><td colspan="2">2561.1</td></tr>
</table>

As shown in Table 3, the measured and the predicted velocities of nylon are 2546 and 2561 m s^{-1}, indicating a good agreement with a difference of around 1%. Lastly, we also explored the effect of the jacket system on acoustic property measurement by comparing the acoustic velocity of water inside the pulse tube and the PVC jacket. We used an empty pulse tube to calculate the water velocity from the propagation time from hydrophone 1 to hydrophone 2. Then, we compared the measured water velocity inside and outside the jacketed sample. The results showed a 3% reduction in velocity due to the jacket system (i.e., 1374 ± 21 and 1419 ± 22 ms^{-1} for water velocity in the PVC jacket and empty pulse tube, respectively). Meanwhile, attenuation shows < 0.001 (or $< 7\%$) difference. For additional comparison, we calculated the acoustic speed in water at 4°C and 10 MPa pressure using equations from Belogol'skii et al. (1999). The theoretical estimate (i.e., 1432 m s^{-1}) is ~1% higher than the acoustic velocity measured in the pulse tube. As a result, we have adopted a calibration factor of 1.03 for measurements using the PVC jacket and estimate that our relative experimental uncertainty is ± 2.4% and ± 5.8% for velocity and attenuation, respectively.

2.4. Theoretical Modelling

The elastic wave properties of water-saturated sediments and rocks can vary significantly with frequency (Williams et al., 2002). Velocity dispersion, i.e., the change in velocity with frequency, is related to attenuation through the principle of causality (e.g., Kolsky, 1956). The velocity and attenuation of elastic waves can be measured over a wide frequency range, including seismic surveys, sonic well-logging, and ultrasonic laboratory experiments. Therefore, it is essential to understand the entire frequency dependence to enable comparison of measurements from various techniques.

Across various theoretical explanations of elastic wave propagation in porous media, particularly unconsolidated sediment, Biot's theory (Biot, 1956a, 1956b) is commonly used (e.g., Cadoret et al., 1998; Chotiros, 1995; Williams et al., 2002). This theory was developed to predict the frequency-dependent velocity and attenuation due to the fluid viscosity and the inertial interaction between pore fluid and sediment matrix. Biot's theory is relevant in unconsolidated sediments (or sand packs) and high-porosity rocks in the high-frequency limit, as opposed to the low-frequency limit (i.e., below 100 Hz) where Gassmann's theory suffices (Gassmann, 1951). Therefore, we compared Biot's model with our laboratory results, in particular the Biot-Stoll model (Stoll and Bryan, 1970) that is incorporated in the hydrate-bearing effective sediment (HBES) model of Marín-Moreno et al. (2017). We used this particular model because it includes additional complex fluid flow mechanisms within the Biot porous medium concept, namely squirt flow and gas bubble interaction.

The HBES model is generally applicable to porous sediments with gas/liquid saturating fluids and does not require hydrate to be present. We used this model (with a hydrate saturation of zero) to predict how gas bubbles affect velocity and attenuation. The model is able to calculate P- and S-wave velocity and attenuation. The model was developed from the Hydrate Effective Grain (HEG) model of Best et al. (2013), which predicts velocity and attenuation dispersion based on the clay-squirt flow mechanism in marine sediment (Leurer, 1997; Leurer and Brown, 2008). This mechanism is incorporated in the Biot-Stoll fluid flow model to predict the frequency-dependent acoustic properties in sediment and rocks as a function of pore content. The HBES model extended the HEG model by adding the effects of gas. The model included gas bubble resonance effects, based on the work of Smeulders and Van Dongen (1997), which makes this model suitable for our study.

To address how pore fluid distribution affected our experimental data, we extended the modelled velocity and attenuation by varying the effective fluid bulk modulus calculated using the Voigt (Voigt, 1889), Brie (Brie et al., 1995) and Reuss (Reuss, 1929) techniques. This extension allowed us to vary the patchiness. In addition, we explored the sensitivity of the results to permeability and gas bubble radius variations. Firstly, we varied the patchiness parameter in the model to match our experimental data using the input parameters in Table 4. Then, we used the best-fit model to explore the permeability and gas bubble radius effects by varying permeability from 0.01 to 10 Darcys and the gas bubble radius from 0.0001 – 10 mm (see Table 5).

Table 4 Fixed input parameters used in the HBES model.

Parameters	**Value**	**Reference**
Effective pressure	10^6 Pa	Experimental setup
Temperature	4°C	
Sand grain properties		
Bulk modulus	36 x 10^9 Pa	Simmons (1965)
Shear modulus	45 x 10^9 Pa	
Density	2650 kgm^{-3}	
Diameter	10^{-4} m	Measured
Coordination number	9	Murphy (1982)
Sand sediment properties		
Porosity	0.41	Measured
Critical porosity	0.38	Best et al. (2013)
Tortuosity	3	Berryman (1981)

Table 5 Gas bubble radius size used in the HBES model.

Gas bubble type	Gas bubble radius (m)
Nanobubble	10^{-7}
Microbubble	10^{-6}, 10^{-5}
Fine bubble	10^{-4}
Medium bubble	10^{-3}
Coarse bubble	10^{-2}

We calculated the difference between the experimental and modelled values to find the best fit using an objective function (Equation 19) at each step of the modelling process. We minimised the objective function to find the best-fit water distribution (patchiness), permeability, and gas bubble radius parameters. When we varied one parameter, we held the other two parameters constant until we found the best fit. For instance, we varied the patchiness parameter first by holding the permeability and gas bubble radius constant.

$$Objective\ function = \frac{\left|V_{experimental} - V_{modelled}\right|}{V_{experimental}} + \frac{\left|Q^{-1}_{experimental} - Q^{-1}_{modelled}\right|}{Q^{-1}_{experimental}} \quad (19)$$

3. Results and Discussion

3.1. Variation of Velocity and Attenuation

P-wave velocity (V_p) increases with frequency across all samples (A-D), with Sample D showing the least variation (Figure 9). Attenuation patterns are more complex: Sample A shows a significant decrease with frequency, Samples B and C exhibit more complex behaviour, and Sample D shows little variation, particularly above 4.5 kHz. There are significant variations with saturation level, particularly in V_p. Fully saturated sand packs consistently show the highest V_p, as expected, while attenuation displays more variation with frequency. Results for each sample at all saturation levels (S_w) are in the Supplementary Information (Figure S5).

We observe V_p peaks in Sample A (12.5-17.5 kHz at S_w = 100%) and Sample B (10-12.5 kHz at S_w = 50%). The variation in Sample A can be attributed to patchiness, as observed by others at full saturation (Dvorkin and Nur, 1998; Tserkovnyak and Johnson, 2002). Sample A also displays increase attenuation in the same frequency range, supporting the interpretation because patchiness may introduce more attenuation (Cadoret et al., 1998). The variation in Sample B can also be attributed to patchy saturation (Figure 3). Higher saturations extend 5-10 cm from the bottom of the sample, which could affect V_p in the frequency range of the peak, where the wavelength is approximately 11 cm. Variations in both velocity and attenuation towards both ends of the frequency spectrum resulting from processing artefacts due to the time-gating process (Section 2.3.2), particularly impacting the lower frequencies, as seen in the case of Sample C below 2.5 kHz.

Velocity and attenuation both increase with saturation at all pressure levels (Figure 10), after a small initial reduction in velocity from S_w = 0% to about S_w = 50%. However, the rate of increase varies, particularly for V_p at S_w = 75-100%, with higher pressures showing larger increases. This trend is due to the compaction of air bubbles within pores near to full saturation, significantly increasing velocity (Dvorkin and Nur, 1998). Attenuation increases similarly with saturation at all pressures. At lower saturation levels (e.g., S_w < 50%), attenuation may be affected by local flow mechanisms; however, at higher saturation, attenuation can be associated with patchy fluid distribution. Additionally, at sufficiently high frequencies (i.e., sonic frequencies), unrelaxed pores can increase attenuation (Cadoret et al., 1998; El-Husseiny et al., 2019; Mavko and Nolen-Hoeksema, 1994).

a)

b)

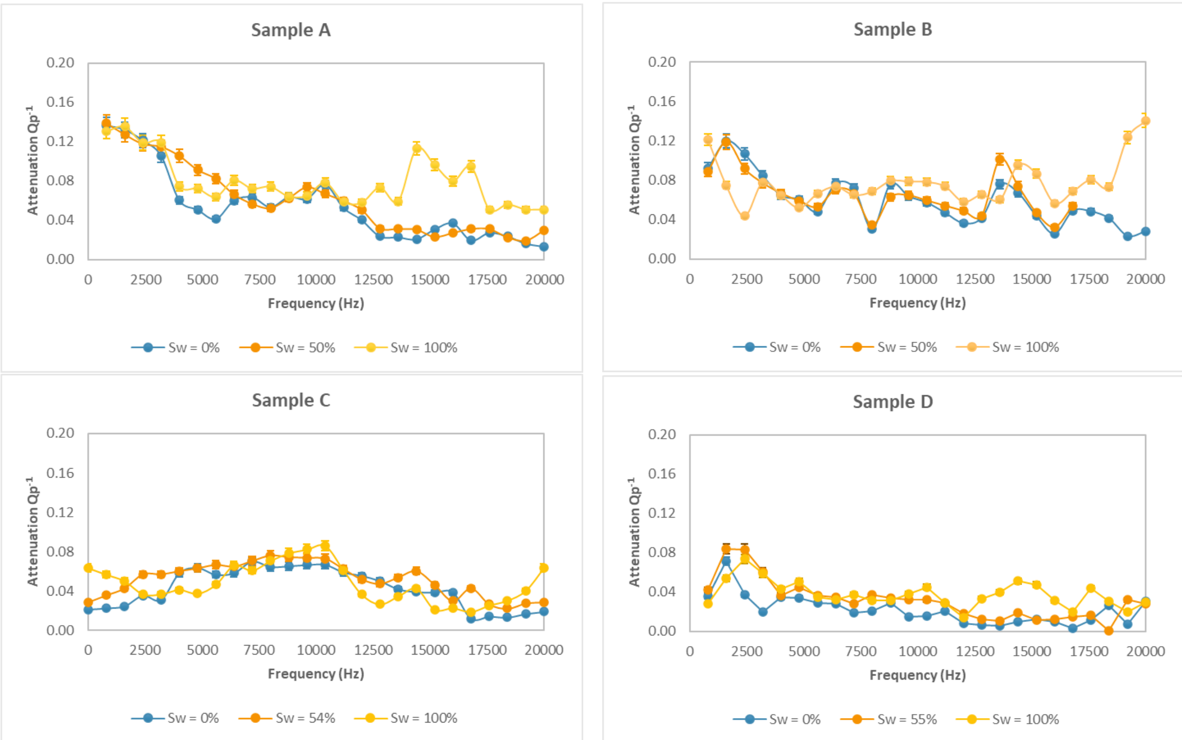

Figure 9 Measured variations in P-wave velocity (V_p) and attenuation (Q_p^{-1}) across the acoustic pulse tube frequency range of 1-20 kHz at three saturation levels: dry (0%), partially saturated (~50-55%), and fully saturated (100%). The effective pressure was 10 MPa and the temperature was 4°C.

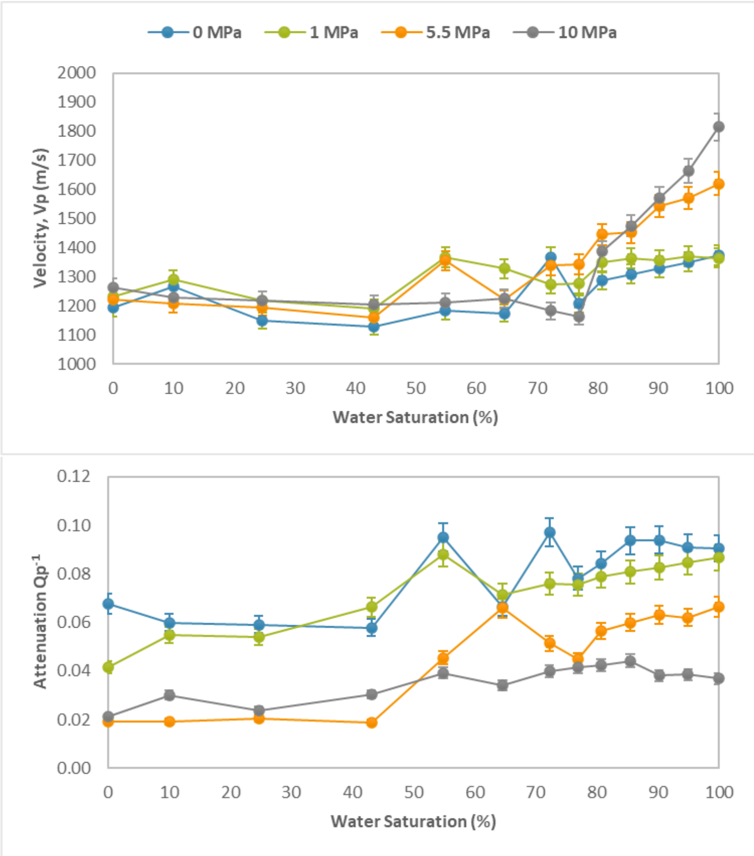

Figure 10 Variation in measured P-wave velocity and attenuation with water saturation at 10 kHz at effective pressures between 0 – 10 MPa indicated in the legend in Sample D at a temperature of 4°C.

P-wave velocity increases and attenuation decreases with increasing effective pressure (Figure 11). Using relative value (compared to the 0 MPa condition), we highlighted the impact of effective pressure on both acoustic parameters. Sample compaction progressively increases from 0 to 10 MPa due to micro-crack closure and grain movement to be a closer pack, reflecting a non-linear V_p trend at S_w = 100% (He et al., 2021; Horikawa et al., 2021; Prasad, 2002). The compaction effect is masked by the fluid distribution effect at intermediate S_w (e.g., S_w = 50% in Figure 11) because the bulk modulus of the samples is dominated by the effective fluid modulus. The dry sample exhibits the greatest attenuation reduction with increasing pressure, particularly from 1 to 5.5 MPa, due to initial cracks closure and reduced gas pocket volumes (e.g., Li et al., 2014; Zhang et al., 2022). In addition, only grain contact squirt flow is present in the dry sample, whereas partial and fully saturated samples also experience other attenuation mechanisms, such as mesoscopic fluid flow, Biot flow, and gas bubble scattering.

In the dry sample, gas predominates in the pores, with residual water present only at grain contacts, in microcracks, and adsorbed on grain surfaces. Fully saturated samples have minimal residual gas saturation. However, in 50% water-saturated samples, two co-existing fluids in the pores lead to gas bubble formation in the water. Gas bubble resonance effects might affect attenuation in 50% water-saturated samples, giving a different trend than dry and fully saturated samples. Pore-scale fluid flow mechanisms might also affect the behaviour at intermediate saturations (Winkler and Nur, 1979; Zhan et al., 2022).

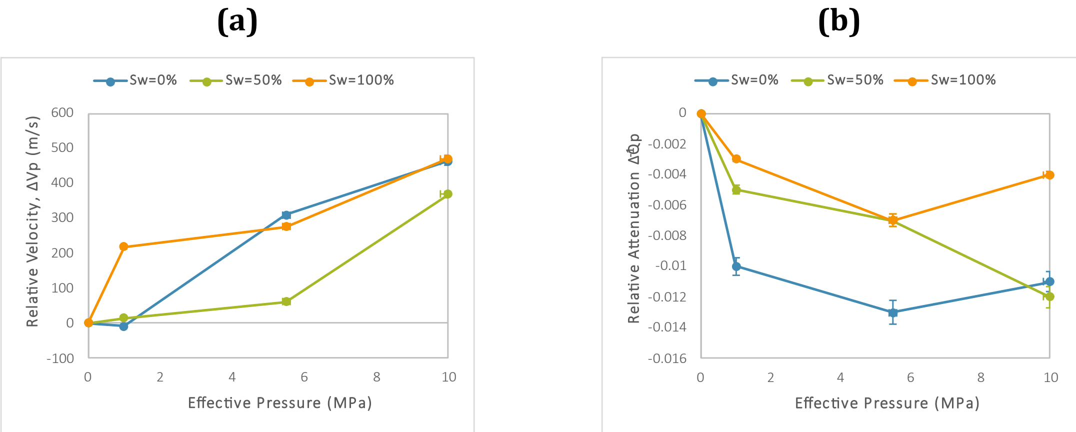

Figure 11 Variations in relative velocity and attenuation with effective pressure at 10 kHz in Sample D at three water saturations of 0%, 50%, and 100%. The velocity and attenuation at 0 MPa were used as the reference values. The temperature was 4°C.

We present data from four samples to explore the water saturation effect on acoustic parameters (Figure 12). V_p consistently decreases with saturation up to S_w ~75%, then increases up to full saturation, with the main differences occurring at S_w > 70%. V_p increases at S_w ~80% for Samples A and D and at S_w ~70% for Samples B and C. However, attenuation varies significantly between samples, with Sample D exhibiting a lower average value.

The V_p variation with saturation resembles that previously observed for homogeneous saturations, characterised by a decrease followed by a sharp increase (e.g., Dvorkin and

Nur, 1998). For homogeneous saturations, the compressibility of the water-gas mixture is similar to that of air across most saturation levels. However, as full saturation is approached (around S_w ~75% in this study), the compressibility of the mixture approaches that of water, leading to a sharp increase in bulk modulus and, consequently, velocity. Attenuation behaviour is influenced by fluid flosw mechanism. At lower saturations (S_w = 0–75%), microscopic fluid flow controls attenuation (Alkhimenkov et al., 2020; Cadoret et al., 1998), while at the highest saturations, macroscopic mechanisms such as the Biot effect dominate. At full saturation, most samples exhibit a decrease in attenuation, attributed to minimal to no fluid movement between pores, reducing energy loss (H. Li et al., 2020; Oh et al., 2011).

a) **b)**

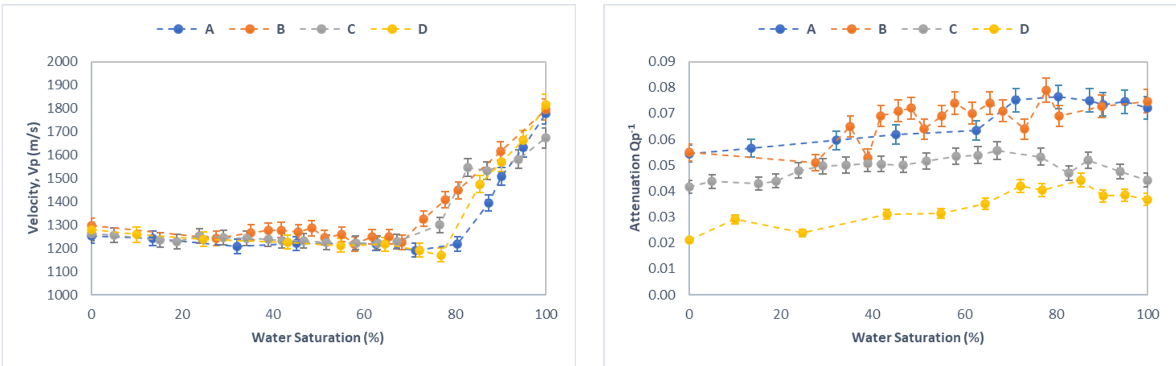

Figure 12 Variations in (a) P-wave velocity and (b) attenuation with water saturation at 10 kHz, for the four samples. The measurements were conducted at an effective pressure of 10 MPa and a temperature of 4°C.

3.2. Comparison with rock physics modelling

3.2.1. Water distribution

The Voigt and Reuss models serve as the upper (patchy saturation) and lower (uniform saturation) bounds for fluid bulk modulus, with Brie's model (Brie et al., 1995) considered a more realistic estimate for patchy saturation (Mavko et al., 2009). We adjusted Brie's calibration constant (e), representing saturation patchiness (Lee and Collett, 2006; Papageorgiou et al., 2016), to fit our experimental data. As e increases, the model approaches uniform saturation, closely resembling the Reuss approximation at e > 30. In contrast, as e decreases, a patchier distribution is represented, closely approaching the Voigt approximation at e = 1.

Our velocity data are better explained by uniform than by patchy gas saturation, with a good fit to the Brie model for *e* ranging from 5 to 10 (Figure 13). From dry to ~75% saturation, the velocity data align well with the *e* = 10 prediction, while at higher saturations (75% - 100%), the best fit lies between *e* = 5 and *e* = 10, suggesting a fluid distribution change as saturation increases. Our attenuation data are better explained by the Brie model with a higher *e* value (*e* > 20), particularly below 70% saturation. At higher saturations, the data are scattered, which complicates the interpretation. Nevertheless, the data from Sample C are closely aligned with the Brie model result for *e* = 10-20. Full plots for all samples can be found in the Supplementary Information (Figure S6).

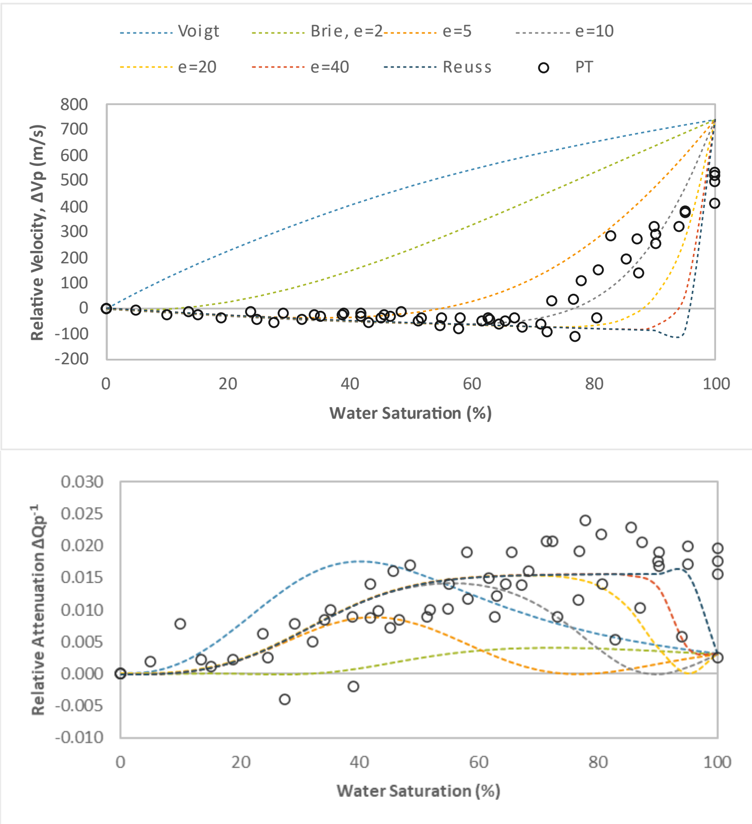

Figure 13 Variations of relative velocity and attenuation with saturation for all samples at 10 kHz, referenced to the measured parameters at S_w=0%, compared to HBES model predictions (with the extension of various fluid bulk modulus approximations) under the permeability of 5 Darcys and gas bubble radius of 0.1 mm. The measurements and predictions were conducted under an effective pressure of 10 MPa and a temperature of 4°C.

3.2.2. Permeability

We explored the effect of permeability changes by varying the model's permeability from 0.01 to 10 Darcy. These simulations are done to match our unconsolidated sand sample data at a centre frequency of 10 kHz, under an effective pressure of 10 MPa, and using Brie's coefficient of e = 10 (Figure 14a). Velocities are higher and vary less with saturation at higher permeabilities, but the differences are too small to be resolved by our data (Figure 14b).

In contrast, attenuation varies significantly with permeability across all saturations (Figure 14a). Attenuation increases with permeability, particularly below 2.5 Darcy, with higher permeabilities shifting the attenuation peak from higher to lower saturations, deviating from our data above 85% saturation. These changes are most noticeable at permeabilities above 5 Darcys. Based on objective function minimisation, our data best align with the model results for a permeability around 5 Darcy which falls within the measured range of 1 – 8.4 Darcys for a clean quartz sand pack (Wei et al., 2022; West, 1995).

3.2.3. Gas bubble radius

Before exploring the gas bubble radius effect on the acoustic properties, we calculated the pore throat size (a) for our samples to determine the applicable radius range. Stoll (1974) found that pore throat size values range from one-sixth to one-seventh of the mean grain diameter (d), while Hovem and Ingram (1979) calculated it as follows: $a = \emptyset d/[3(1-\emptyset)]$, where $\emptyset$ represents the porosity. Employing both approaches, the result is 0.014 – 0.017 mm.

We used six gas bubble sizes to represent various bubble types (Table 5). However, the results are indistinguishable below 1 mm radius, with significant differences only for the 10 mm radius (Figure 15), which is much larger than the calculated pore throat size. The model predictions with a larger gas bubble radius also deviate from our pulse tube data. Through objective function minimisation, we determined that the best-fitting gas bubble radius is around 0.001 – 0.01 mm, with a 0.1 mm radius also fitting well. Therefore, our data are consistent with bubble sizes no larger than 0.1 mm, explaining the lack of discernible gas bubble resonance effects on attenuation around our simulated gas bubble sizes, especially at 10 kHz (Gong et al., 2010).

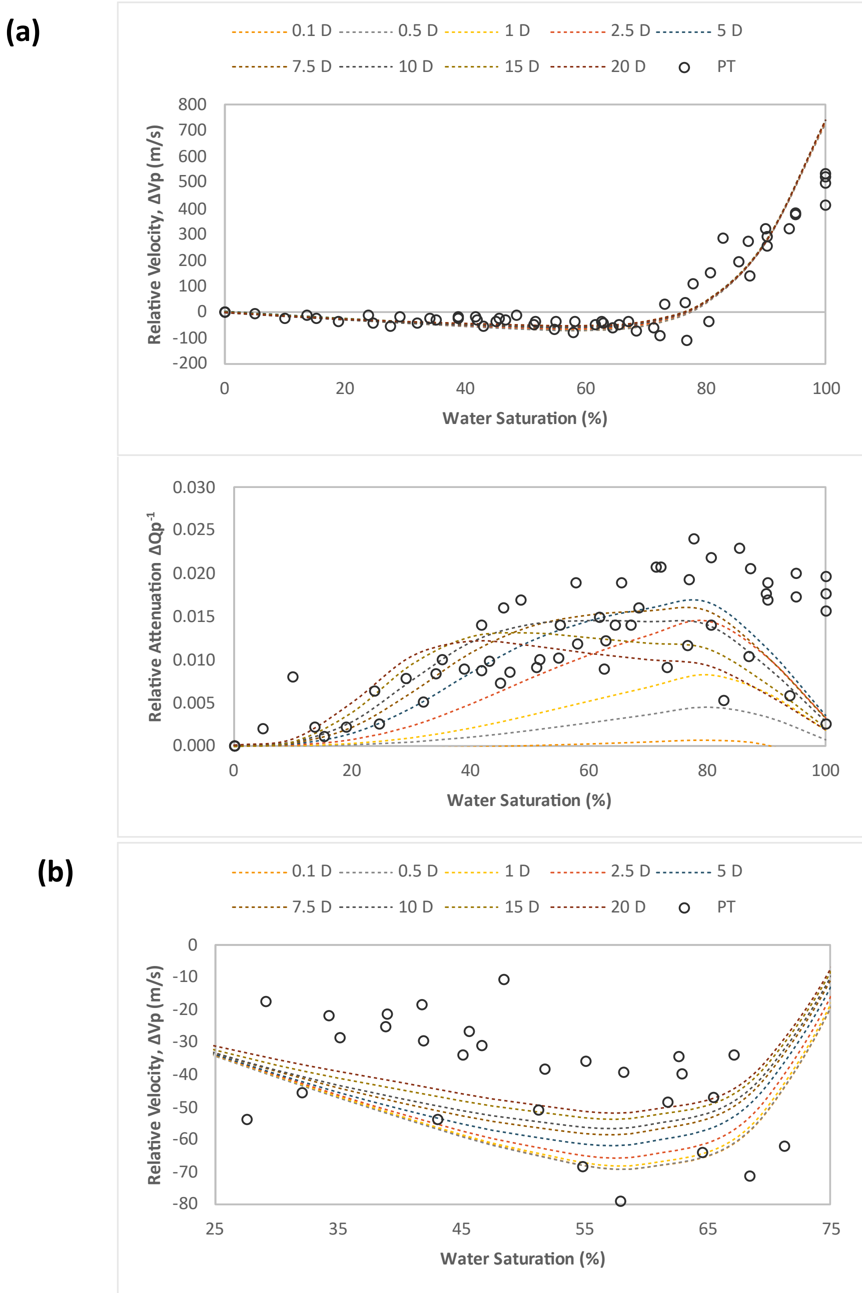

Figure 14 a) Variations of relative velocity and attenuation with saturation for all samples at 10 kHz, referenced to the measured parameters at S_w=0%, compared to the HBES model at various permeabilities. b) The same models and data plotted with an expanded vertical scale. The measurements and simulations were conducted at an effective pressure of 10 MPa and a temperature of 4°C.

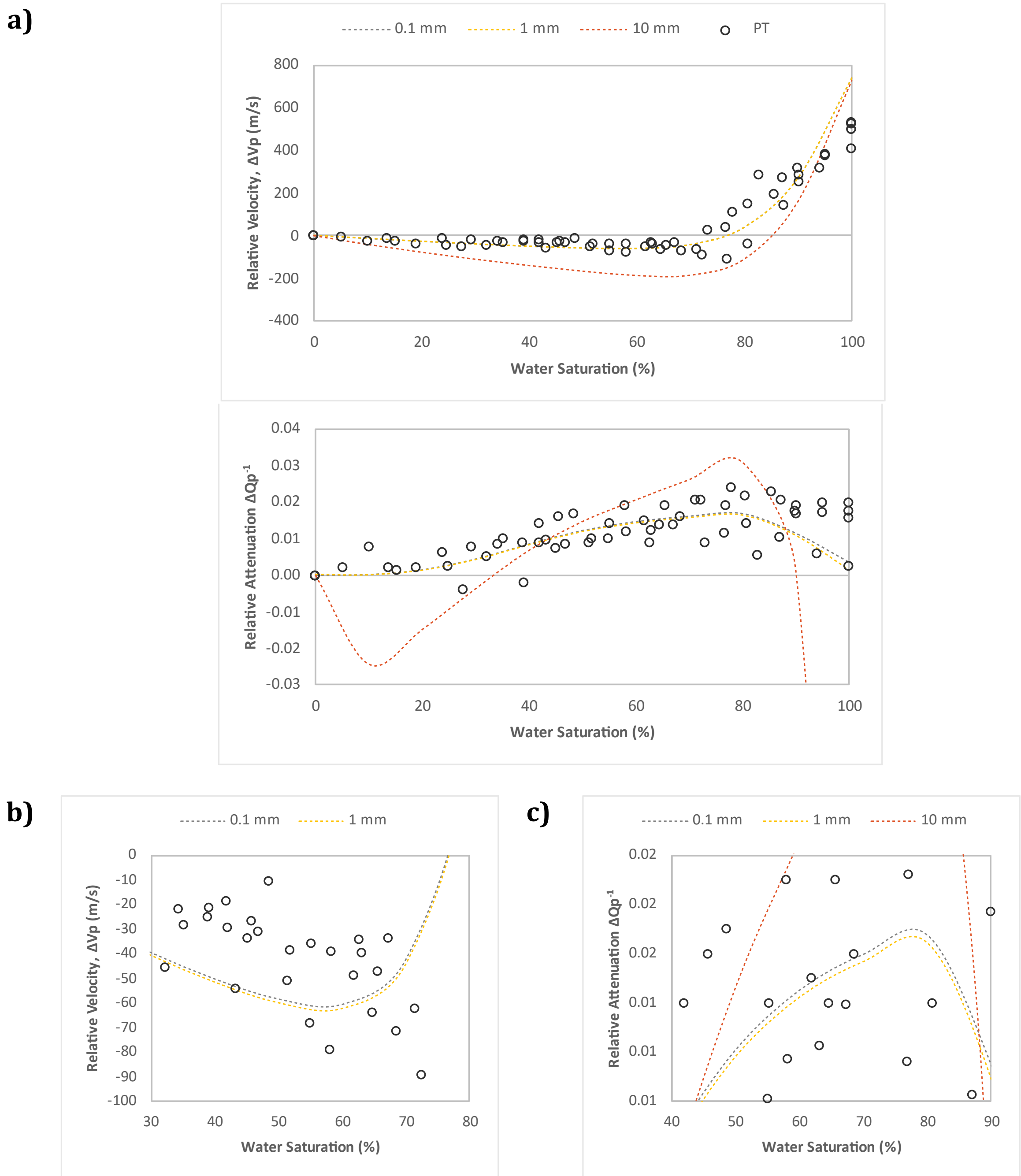

Figure 15 a) Variations of relative velocity and attenuation with saturation for all samples at 10 kHz, referenced to the measured parameters at S_w=0%, compared to the HBES model at various gas bubble radii. b) and c) The same models and data plotted with an expanded vertical scale. The 0.0001 – 0.01 mm results are not shown because they are indistinguishable from the 0.1 mm results. The measurements and simulations were conducted at an effective pressure of 10 MPa and a temperature of 4°C.

3.3. Limitation of study and future direction

We selected a sample size that ensured that the sample length (i.e., 0.5 m) extended at least half of the wavelength at the lowest frequency, which for a velocity of 1200-1300 m s^{-1} is 0.75-0.81 m at 1.6 kHz so that the measurements captured well the sample characteristics. We conducted these lab experiments to imitate natural conditions as closely as possible and to inform field measurements and the development of robust inversion techniques. However, our experiments focus on a single sand pack, whereas field conditions may involve variations in grain size distribution and lithology. In addition, field conditions may include different types of gases with various saturations as part of the pore fluid. Also, we observe variations, particularly in attenuation, that can be attributed to changes in the distribution of pore fluid within the sample. These limitations highlight potential directions for future research.

4. Conclusion

This study presents novel laboratory experimental measurements of P-wave velocity and attenuation Q_p^{-1} on four quartz sand packs in the frequency range 1 – 20 kHz. We conducted the experiments at mostly an effective pressure of 10 MPa and temperature 4°C as a function of air/water saturation using a novel, bespoke acoustic pulse tube. The method provides consistent measurements for PVC-jacketed samples accurate to ± 2.4 % and ± 5.8 % for velocity and attenuation, respectively. We investigated the acoustic properties under varying frequencies, effective pressures, and water saturations. Velocity consistently increases with frequencies, while attenuation patterns vary across samples.

Velocity increases with effective pressure and attenuation decreases, at all water saturations. Dry and fully saturated samples show more pronounced velocity increases than partially saturated ones, while the dry samples show the largest attenuation decreases. Velocities decrease with increasing saturation until around 75% saturation and then increase towards full saturation. In contrast, attenuation initially increases with saturation and later slightly decreases towards full saturation.

We also looked at the effects of patchy saturation, permeability, and gas bubble resonance by comparing predictions from theoretical models to our experimental results. Our samples match better with more uniform saturation models, as represented by $5 < e < 20$ in Brie et al.'s (1995) equation. Our data are best matched using a permeability of around 5 Darcys, which is a reasonable value for unconsolidated fine sand. Our data are matched by a gas bubble radius no higher than 0.1 mm. Table 6 summarises the key findings from the experiments and modelling.

These results offer valuable insights into understanding elastic wave measurements in a broad frequency spectrum. The pulse tube used in this study is a laboratory measurement system working in the sonic frequency range, which can fill the gap in laboratory scale measurements in the sonic frequency range.

Table 6 Summary of the experiments and modelling key findings on acoustic properties to tested parameters.

Parameters	Velocity	Attenuation Q^{-1}
Experimental data analysis		
Frequency	Generally increased, particularly at full water saturation.	Complex relationship, but mainly decreased to slight variation.
Effective pressure	Increased, particularly in dry and full water saturation.	Decreased with significant reduction from 1 to 5.5 MPa*.
Water saturation	Decreased until around 75% saturation, then increased until full saturation.	Increased until around 75% saturation, then slightly decreased until full saturation**.
Modelling comparisons		
Water distribution	The experimental data matched well with the tested model using Brie approximation (*e*=10).	
Permeability	The experimental data matched well with the tested model using a permeability value of 5 Darcys.	
Gas bubble radius	The experimental data matched well with the tested model using gas bubble radius values from 0.0001 - 0.1 mm.	

* Based on tested effective pressure steps, i.e., 0, 1, 5.5, and 10 MPa.

** One sample showed little to no variation from 75% to full saturation.

Acknowledgements

Financial support from the Indonesian Endowment Fund for Education (*Lembaga Pengelola Dana Pendidikan, LPDP)* is gratefully acknowledged. We acknowledge funding from the UK Natural Environment Research Council (NERC) for the acoustic pulse tube (Grant NE/J020753/1). Sahoo was supported by NOC RISC funding (Project No P11828). We also thank the reviewers and editors for their valuable comments, resulting in the improvement of this manuscript.

Data Availability Statement

Data associated with this research are available and can be obtained by contacting the corresponding author.

References

Alkhimenkov, Y., Caspari, E., Gurevich, B., Barbosa, N.D., Glubokovskikh, S., Hunziker, J., Quintal, B., 2020. Frequency-dependent attenuation and dispersion caused by squirt flow: Three-dimensional numerical study. GEOPHYSICS 85, MR129–MR145. https://doi.org/10.1190/geo2019-0519.1

Asada, M., Satoh, M., Tanahashi, M., Yokota, T., Goto, S., 2022. Visualization of shallow subseafloor fluid migration in a shallow gas hydrate field using high-resolution acoustic mapping and ground-truthing and their implications on the formation process: a case study of the Sakata Knoll on the eastern margin of the Sea of Japan. Mar. Geophys. Res. 43, 34. https://doi.org/10.1007/s11001-022-09495-9

ASTM, 2007. Standard Test Methods for Laboratory Compaction Characteristics of Soil Using Standard Effort, ASTM Standard D698. ASTM International.

Ayres, A., Theilen, F., 2001. Preliminary laboratory investigations into the attenuation of compressional and shear waves on near-surface marine sediments: Attenuation of P- and S-waves. Geophys. Prospect. 49, 120–127. https://doi.org/10.1046/j.1365-2478.2001.00243.x

Azuma, H., Konishi, C., Xue, Z., 2013. Introduction and Application of the Modified Patchy Saturation for Evaluating CO2 Saturation by Seismic Velocity. Energy Procedia 37, 4024–4032. https://doi.org/10.1016/j.egypro.2013.06.302

Barriere, J., Bordes, C., Brito, D., Senechal, P., Perroud, H., 2012. Laboratory monitoring of P waves in partially saturated sand. Geophys. J. Int. https://doi.org/10.1111/j.1365-246X.2012.05691.x

Batzle, M.L., Han, D.-H., Hofmann, R., 2006. Fluid mobility and frequency-dependent seismic velocity — Direct measurements. GEOPHYSICS 71, N1–N9. https://doi.org/10.1190/1.2159053

Belogol'skii, V.A., Sekoyan, S.S., Samorukova, L.M., Stefanov, S.R., Levtsov, V.I., 1999. Pressure dependence of the sound velocity in distilled water. Meas. Tech. 42, 406–413. https://doi.org/10.1007/BF02504405

Berryman, J.G., 1981. Elastic wave propagation in fluid-saturated porous media II. J. Acoust. Soc. Am. 70, 1754–1756. https://doi.org/10.1121/1.387193

Best, A.I., Priest, J.A., Clayton, C.R.I., Rees, E.V.L., 2013. The effect of methane hydrate morphology and water saturation on seismic wave attenuation in sand under shallow sub-seafloor conditions. Earth Planet. Sci. Lett. 368, 78–87. https://doi.org/10.1016/j.epsl.2013.02.033

Biot, M.A., 1956a. Theory of Propagation of Elastic Waves in a Fluid-Saturated Porous Solid. I. Low-Frequency Range. J. Acoust. Soc. Am. 28, 168–178. https://doi.org/10.1121/1.1908239

Biot, M.A., 1956b. Theory of Propagation of Elastic Waves in a Fluid-Saturated Porous Solid. II. Higher Frequency Range. J. Acoust. Soc. Am. 28, 179–191. https://doi.org/10.1121/1.1908241

Bouzidi, Y., Schmitt, D.R., 2009. Measurement of the speed and attenuation of the Biot slow wave using a large ultrasonic transmitter. J. Geophys. Res. 114, B08201. https://doi.org/10.1029/2008JB006018

Brie, A., Pampuri, F., Marsala, A.F., Meazza, O., 1995. Shear Sonic Interpretation in Gas-Bearing Sands. Presented at the SPE Annual Technical Conference and Exhibition, p. SPE-30595-MS. https://doi.org/10.2118/30595-MS

Cadoret, T., Mavko, G., Zinszner, B., 1998. Fluid distribution effect on sonic attenuation in partially saturated limestones. GEOPHYSICS 63, 154–160. https://doi.org/10.1190/1.1444308

Chapman, S., Borgomano, J.V.M., Quintal, B., Benson, S.M., Fortin, J., 2021. Seismic Wave Attenuation and Dispersion Due to Partial Fluid Saturation: Direct Measurements and Numerical Simulations Based on X-Ray CT. J. Geophys. Res. Solid Earth 126. https://doi.org/10.1029/2021JB021643

Chotiros, N.P., 1995. Biot model of sound propagation in water-saturated sand. J. Acoust. Soc. Am. 97, 17. https://doi.org/10.1121/1.412304

Dong, J., Sun, H., Zou, D., Yang, H., Jiang, Y., Liu, W., Kan, G., 2023. Model and prediction relationship of sound velocity and porosity of seafloor sediments. J. Sea Res. 194, 102413. https://doi.org/10.1016/j.seares.2023.102413

Dubbelday, P.S., Capps, R.N., 1984. Interpretation of sample wave speed measured in an impedance tube. J. Acoust. Soc. Am. 76, 964–967. https://doi.org/10.1121/1.391217

Dvorkin, J., Nur, A., 1998. Acoustic signatures of patchy saturation. Int. J. Solids Struct. 35, 4803–4810. https://doi.org/10.1016/S0020-7683(98)00095-X

El-Husseiny, A., Vega, S., Nizamuddin, S., 2019. The effect of pore structure complexity and saturation history on the variations of acoustic velocity as function of brine and oil saturation in carbonates. J. Pet. Sci. Eng. 179, 180–191. https://doi.org/10.1016/j.petrol.2019.04.019

Ellingsrud, S., Eidesmo, T., Johansen, S., Sinha, M.C., MacGregor, L.M., Constable, S., 2002. Remote sensing of hydrocarbon layers by seabed logging (SBL): Results from a cruise offshore Angola. Lead. Edge 21, 972–982. https://doi.org/10.1190/1.1518433

Fawad, M., Mondol, N.H., 2021. Monitoring geological storage of CO2: a new approach. Sci. Rep. 11, 5942. https://doi.org/10.1038/s41598-021-85346-8

Ghodgaonkar, D.K., Varadan, V.V., Varadan, V.K., 1990. Free-space measurement of complex permittivity and complex permeability of magnetic materials at microwave frequencies. IEEE Trans. Instrum. Meas. 39, 387–394. https://doi.org/10.1109/19.52520

Glasser, L.A., 1978. An Analysis of Microwave De-Embedding Errors (Technical Notes). IEEE Trans. Microw. Theory Tech. 26, 379–380. https://doi.org/10.1109/TMTT.1978.1129395

Gong, Y., Cabodi, M., Porter, T., 2010. Pressure-dependent Resonance Frequency for Lipid-coated Microbubbles at Low Acoustic Pressures.

Guerin, G., Goldberg, D., 2005. Modeling of acoustic wave dissipation in gas hydrate-bearing sediments: ACOUSTIC WAVE DISSIPATION. Geochem. Geophys. Geosystems 6, n/a-n/a. https://doi.org/10.1029/2005GC000918

He, W., Chen, Z., Shi, H., Liu, C., Li, S., 2021. Prediction of acoustic wave velocities by incorporating effects of water saturation and effective pressure. Eng. Geol. 280, 105890. https://doi.org/10.1016/j.enggeo.2020.105890

Horikawa, T., Katsura, M., Yokota, T., Nakashima, S., 2021. Effects of pore water distributions on *P* -wave velocity–water saturation relations in partially saturated sandstones. Geophys. J. Int. 226, 1558–1573. https://doi.org/10.1093/gji/ggab143

Hovem, J.M., Ingram, G.D., 1979. Viscous attenuation of sound in saturated sand. J. Acoust. Soc. Am. 66, 1807–1812. https://doi.org/10.1121/1.383653

Jedari-Eyvazi, F., Bayrakci, G., Minshull, T.A., Bull, J.M., Henstock, T.J., Macdonald, C., Robinson, A.H., 2023. Seismic characterization of a fluid escape structure in the North Sea: the Scanner Pockmark complex area. Geophys. J. Int. 234, 597–619. https://doi.org/10.1093/gji/ggad078

Klimentos, T., McCann, C., 1988. Attenuation of compressional waves in water?saturated sandstones by intra?pore clay minerals, in: SEG Technical Program Expanded Abstracts 1988, SEG Technical Program Expanded Abstracts. Society of Exploration Geophysicists, pp. 933–935. https://doi.org/10.1190/1.1892402

Le, T.M.H., Eiksund, G.R., Strøm, P.J., Saue, M., 2014. Geological and geotechnical characterisation for offshore wind turbine foundations: A case study of the Sheringham Shoal wind farm. Eng. Geol. 177, 40–53. https://doi.org/10.1016/j.enggeo.2014.05.005

Lee, M.W., Collett, T.S., 2006. Proceedings of the Ocean Drilling Program, 199 Scientific Results, Proceedings of the Ocean Drilling Program. Ocean Drilling Program. https://doi.org/10.2973/odp.proc.sr.199.2006

Leurer, K.C., 1997. Attenuation in fine-grained marine sediments: Extension of the Biot-Stoll model by the “effective grain model” (EGM). GEOPHYSICS 62, 1465–1479. https://doi.org/10.1190/1.1444250

Leurer, K.C., Brown, C., 2008. Acoustics of marine sediment under compaction: Binary grain-size model and viscoelastic extension of Biot’s theory. J. Acoust. Soc. Am. 123, 1941–1951. https://doi.org/10.1121/1.2871839

Li, H., Zhao, L., Han, D., Gao, J., Yuan, H., Wang, Y., 2020. Experimental study on frequency-dependent elastic properties of weakly consolidated marine sandstone: effects of partial saturation. Geophys. Prospect. https://doi.org/10.1111/1365-2478.13031

Li, J., Roche, B., Bull, J.M., White, P.R., Davis, J.W., Deponte, M., Gordini, E., Cotterle, D., 2020. Passive acoustic monitoring of a natural CO2 seep site – Implications for carbon capture and storage. Int. J. Greenh. Gas Control 93, 102899. https://doi.org/10.1016/j.ijggc.2019.102899

Li, X., Dong, L., Zhao, Q., 2014. Seismic modelling study of P-wave attenuation and velocity dispersion in patchy-saturated porous media. J. Geophys. Eng. 11, 065010. https://doi.org/10.1088/1742-2132/11/6/065010

Marín-Moreno, H., Sahoo, S.K., Best, A.I., 2017. Theoretical modeling insights into elastic wave attenuation mechanisms in marine sediments with pore-filling methane hydrate: Hydrate-Bearing Effective Sediment Model. J. Geophys. Res. Solid Earth. https://doi.org/10.1002/2016JB013577

Mavko, G., Mukerji, T., Dvorkin, J., 2009. The Rock Physics Handbook, 2nd ed. Cambridge University Press.

Mavko, G., Nolen-Hoeksema, R., 1994. Estimating seismic velocities at ultrasonic frequencies in partially saturated rocks. Geophysics 59, 252–258.

McCann, C., Sothcott, J., Best, A.I., 2014. A new laboratory technique for determining the compressional wave properties of marine sediments at sonic frequencies and *in situ* pressures: Compressional wave properties of marine sediments. Geophys. Prospect. 62, 97–116. https://doi.org/10.1111/1365-2478.12079

McPhee, C., Reed, J., Zubizarreta, I., 2015. Chapter 9 - Capillary Pressure, in: McPhee, C., Reed, J., Zubizarreta, I. (Eds.), Core Analysis, Developments in Petroleum Science. Elsevier, pp. 449–517. https://doi.org/10.1016/B978-0-444-63533-4.00009-3

Murphy, W.F., 1982. Effects of partial water saturation on attenuation in Massilon sandstone and Vycor porous glass. J. Acoust. Soc. Am. 71, 1458–1468. https://doi.org/10.1121/1.387843

Oh, T.-M., Kwon, T.-H., Cho, G.-C., 2011. Effect of Partial Water Saturation on Attenuation Characteristics of Low Porosity Rocks. Rock Mech. Rock Eng. 44, 245–251. https://doi.org/10.1007/s00603-010-0121-6

Papageorgiou, G., Amalokwu, K., Chapman, M., 2016. Theoretical derivation of a Brie-like fluid mixing law: Brie-like fluid mixing law. Geophys. Prospect. 64, 1048–1053. https://doi.org/10.1111/1365-2478.12380

Prasad, M., 2002. Acoustic measurements in unconsolidated sands at low effective pressure and overpressure detection. GEOPHYSICS 67, 405–412. https://doi.org/10.1190/1.1468600

Pride, S.R., Berryman, J.G., Harris, J.M., 2004. Seismic attenuation due to wave-induced flow: WAVE-INDUCED FLOW LOSSES. J. Geophys. Res. Solid Earth 109. https://doi.org/10.1029/2003JB002639

Reuss, A., 1929. Berechnung der Fließgrenze von Mischkristallen auf Grund der Plastizitätsbedingung für Einkristalle . ZAMM - Z. Für Angew. Math. Mech. 9, 49–58. https://doi.org/10.1002/zamm.19290090104

Reynolds, J., Catt, L., Salaün, G., Knight, P., Cleverly, W., Costa, L., 2017. Integration of Geophysical, Geological and Geotechnical Data for Offshore Wind Farms East Anglia One OWF, Southern North Sea, A Case History. Offshore Site Investig. Geotech. 8th Int. Conf. Proceeding 1291–1298. https://doi.org/doi:10.3723/OSIG17.1291

Richards, S., Tan, A., Platt, I., Woodhead, I., 2014. Free-space microwave moisture content measurement of moist sand, in: 2014 IEEE Sensors Applications Symposium (SAS). Presented at the 2014 IEEE Sensors Applications Symposium (SAS), IEEE, Queenstown, New Zealand, pp. 145–150. https://doi.org/10.1109/SAS.2014.6798935

Sahoo, S.K., Best, A.I., 2021. The Influence of Gas Hydrate Morphology on Reservoir Permeability and Geophysical Shear Wave Remote Sensing. J. Geophys. Res. Solid Earth 126. https://doi.org/10.1029/2021JB022206

Schumann, K., Stipp, M., Behrmann, J.H., Klaeschen, D., Schulte-Kortnack, D., 2014. *P* and *S* wave velocity measurements of water-rich sediments from the Nankai Trough, Japan: P- and S-wave velocity measurements. J. Geophys. Res. Solid Earth 119, 787–805. https://doi.org/10.1002/2013JB010290

Selfridge, A.R., 1985. Approximate Material Properties in Isotropic Materials. IEEE Trans. Sonics Ultrason. 32, 381–394. https://doi.org/10.1109/T-SU.1985.31608

Simmons, G., 1965. Single Crystal Elastic Constants and Calculated Aggregate Properties 274.

Smeulders, D.M.J., Van Dongen, M.E.H., 1997. Wave propagation in porous media containing a dilute gas–liquid mixture: theory and experiments. J. Fluid Mech. 343, 351–373. https://doi.org/10.1017/S0022112097005983

Stoll, R.D., 1985. Marine sediment acoustics. J. Acoust. Soc. Am. 77, 12. https://doi.org/10.1121/1.391928

Stoll, R.D., 1974. Acoustic Waves in Saturated Sediments. Presented at the Physics of Sound in Marine Sediments, pp. 19–39.

Stoll, R.D., Bryan, G.M., 1970. Wave Attenuation in Saturated Sediments. J. Acoust. Soc. Am. 47, 1440–1447. https://doi.org/10.1121/1.1912054

Tserkovnyak, Y., Johnson, D.L., 2002. Can one hear the shape of a saturation patch? Geophys. Res. Lett. 29. https://doi.org/10.1029/2001GL014709

Voigt, W., 1889. Ueber die Beziehung zwischen den beiden Elasticitätsconstanten isotroper Körper. Ann. Phys. 274, 573–587. https://doi.org/10.1002/andp.18892741206

Wei, J., Li, J., Zhang, X., Wang, Z., Shi, J., Huang, Z., 2022. Experimental investigation for the dynamic adsorption behaviors of gel system with long slim sandpack: Implications for enhancing oil recovery. Energy Rep. 8, 9270–9278. https://doi.org/10.1016/j.egyr.2022.07.057

West, T.R., 1995. Geology Applied to Engineering, 1st Edition. ed. Prentice-Hall.

White, J.E., 1975. COMPUTED SEISMIC SPEEDS AND ATTENUATION IN ROCKS WITH PARTIAL GAS SATURATION. GEOPHYSICS 40, 224–232. https://doi.org/10.1190/1.1440520

Williams, K.L., Jackson, D.R., Thorsos, E.I., Dajun Tang, Schock, S.G., 2002. Comparison of sound speed and attenuation measured in a sandy sediment to predictions based on the Biot theory of porous media. IEEE J. Ocean. Eng. 27, 413–428. https://doi.org/10.1109/JOE.2002.1040928

Winkler, K., Nur, A., 1979. Pore fluids and seismic attenuation in rocks. Geophys. Res. Lett. 6, 1–4. https://doi.org/10.1029/GL006i001p00001

Zhan, L., Liu, B., Zhang, Y., Lu, H., 2022. Rock Physics Modeling of Acoustic Properties in Gas Hydrate-Bearing Sediment. J. Mar. Sci. Eng. 10, 1076. https://doi.org/10.3390/jmse10081076

Zhang, Q., Liu, X., He, T., Lu, H., 2022. Influence of Gas Hydrate on the Acoustic Properties of Sediment: A Comprehensive Review with a Focus on Experimental Measurements. Acta Geol. Sin. - Engl. Ed. 96, 713–726. https://doi.org/10.1111/1755-6724.14932